On the Use of HF Surface Wave Radar in Congested Waters: Influence of Masking Effect on Detection of Small Ships

Régis Guinvarc'h, *Member, IEEE*, Marc Lesturgie, Rémi Durand, and Anil Cheraly

***Abstract*—In this paper, we assess the capability of a high-frequency surface wave radar (HFSWR) to detect a small fast boat moving behind a ship, the dimensions of which are comparable to the wavelength. We show that, in the HF-band, the scattered field in the shadow region of the large ship is significant enough to induce strong coupling between the two vessels. This results in fluctuations in the radar cross section (RCS) values of the small boat of about 12 dB at 10 MHz, for instance. We also introduce a complete simulation tool to account for the environment and, thus, to be able to simulate real scenes. We have validated these results through anechoic chamber measurements, with two different masking vessels and three different masked ships. The measurements have shown both the low-attenuation results and the RCS fluctuations.**

***Index Terms*—Diffraction, high-frequency surface wave radar (HFSWR).**

I. Introduction

MARITIME surveillance around congested waters is a priority, as testified by the resurgence of a once-disappearing menace: piracy. Pirate attacks worldwide increased in frequency and violence last year, with a total of 445 incidents reported compared with 370 in 2002 [1]. Another big problem that has to be pointed out is smuggling. Both pirates and arms or drugs dealers use boats with low radar cross section (RCS) that can go at very high speed.

The detection of these small fast boats (SFB) is a challenge, due to low RCS. When they are behind big vessels, this detection becomes almost impossible if only microwaves are considered. High-frequency surface waves radar (HFSWR) is a well-known solution to cope with the line of sight limitation in maritime surveillance. However, performances of HFSWR are usually considered and validated under the assumption that the propagation path along the earth curvature is free of any obstacle. This configuration cannot be assumed for a coastal radar installed in congested waters such as straits and ports which generate high maritime traffic. Along the coasts of such areas, an endless queue of very large vessels, such as tankers, container ships, and so on, can then be observed. Due to the huge dimensions of these vessels (more than 100-m long for most of them, with about 20-m height), they form a kind of electromagnetic barrier, hiding most of the sea surface to the conventional, i.e., X-band, coastal radars.

The first part of this paper reviews the design of an HFSWR dedicated to maritime surveillance. The second part of this paper describes the modeling of diffraction effects created by a masking vessel on a small ship. Modeling results, performed in the high-frequency (HF)-band, are analyzed in term of propagation loss in coupling effect. Bistatic RCS is also analyzed. The modeling approach is finally completed by a realistic model of surface wave. The last part of this paper deals with an experimental validation, from anechoic chamber measurement performed on different scaled model (oil tanker, fishing boat, small ship, etc.).

Manuscript received November 25, 2004; accepted September 1, 2006. **Associate Editor: M. L. Heron**.

The authors are with Supelec ONERA NUS DSTA Research Alliance (SONDRA), Gif-Sur-Yvette 91192, France (e-mail: regis.guinvarch@ieee.org).

Digital Object Identifier 10.1109/JOE.2006.886227

II. Detection of Ship by HFSWR

The detection of ship targets by HFSWR is mainly based on Doppler processing. Detection performances depend both on sea clutter Doppler spectrum and target Doppler shift. Assuming that the thermal noise is much lower than the clutter level, the detection performance can be simply approached using a target-to-clutter ratio (TCR)

$$\mathrm{TCR} = \frac{\sigma}{\sigma^{00}\delta\theta R\delta r} \tag{1}$$

with

- σ RCS of the target (unit: m^2/m^2);
- σ^{00} clutter reflectivity (unit: m^2/m^2);
- R target range;
- $\delta\theta$ azimuth resolution;
- δr radar range resolution.

The clutter reflectivity is composed of first and second orders of the Bragg phenomenon. The second-order reflectivity must be considered for a given value of the coherent integration time. TCR has to be optimized with respect of the critical sizing parameters of the radar. In particular, selection of the carrier frequency should be addressed with attention to the following.

- In the lower part of HF-band (typically between 4–10 MHz), the second-order reflectivity of the sea is low since the roughness is low, compared to the large radar wavelength; however, the target RCS is also very low; azimuth and radial velocity resolutions are also poor.
- In the higher part of HF-band (typically between 10–30 MHz), the second order of sea clutter reflectivity becomes important; however, the target RCS increases and

0364-9059/$20.00 © 2006 IEEE

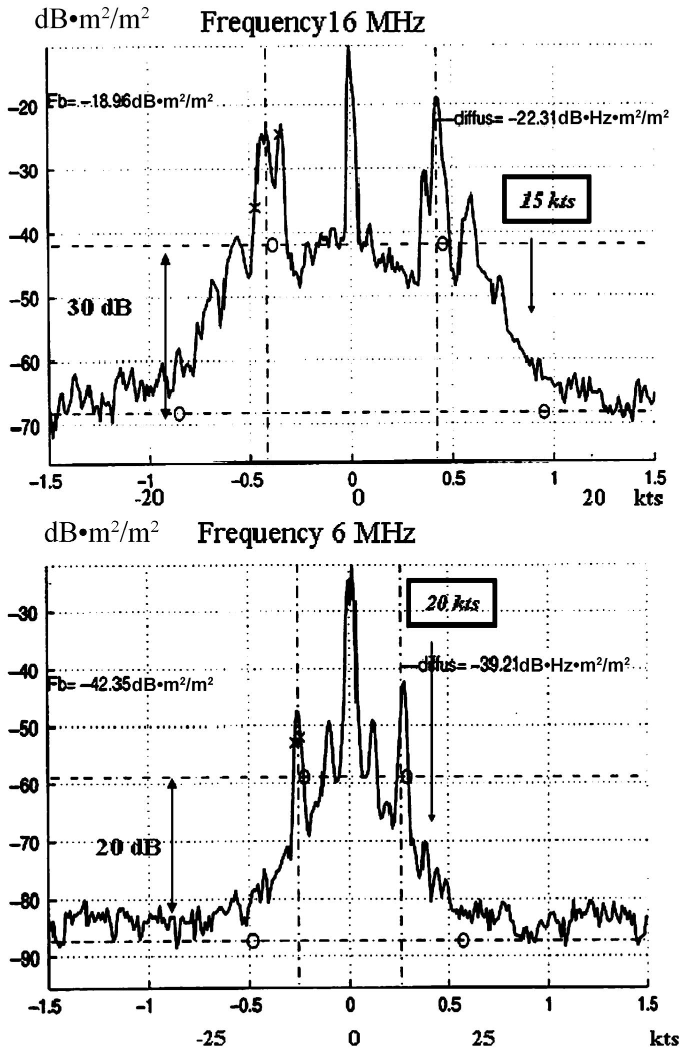

Fig. 1. Coastal measurements at 16 and 6 MHz in Mediterranean sea. Low RCS values.

interesting azimuth and radial velocity resolution can be obtained.

To illustrate the dependence of sea clutter on frequency, Fig. 1 depicts two experimental spectra obtained at 6 and 16 MHz. Second-order level is lower at 6 MHz (-60 dB$\cdot$m^2/m^2) than at 16 MHz (-40 dB$\cdot$m^2/m^2). However, a fast target (more than 15 kt) can be more easily detected at 16 MHz since the Doppler shift is no longer jammed by sea clutter. The experimental coastal HFSW radar was operating in the Mediterranean sea in France. The absolute level of sea clutter (at 6 and 16 MHz) appears as low as levels usually obtained in open seas (or oceans); coastal effects in a closed sea lead to reducing the dynamic of sea waves. Interesting comparisons between open and close seas can be found in [2].

A. Detection Performance of HFSWR on Ship Target

Conventional HFSWR uses a quasi-monostatic configuration; the transmitting unit (Tx) is based on a single or a couple of log-periodic dipole array (LPDA) antennas for example and the receiving unit (Rx) is based on a wide array of antennas (for example passive monopole antennas). Rx and Tx units are separated due to different requirements. The Rx array must provide a narrowbeam to reduce the clutter area while the Tx must transmit the maximum level of power in a wide sector of surveillance. This is illustrated in Fig. 2.

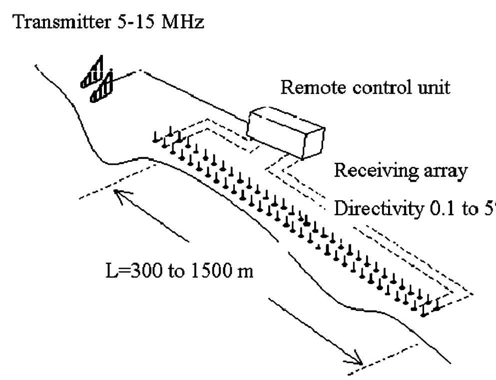

Fig. 2. HFSWR.

HFSWR performances, in terms of maximum detection range (for a given target), can be easily approached through the conventional concept of radar equation when the target presents a Doppler shift greater than the clutter interval. For targets embedded in the clutter spectrum, performances are deduced from the target to clutter ratio.

Optimization of radar performances in this case can be achieved by minimizing the second-order reflectivity σ^{00} (using a lower frequency, between 4–8 MHz, for example), decreasing the azimuth resolution $\delta\theta$ (using a much longer receiving antenna array) and reducing the range resolution δr (using an higher frequency bandwidth). Based on conventional orders of magnitude for the different parameters (RCS between 10 and 40 dB$\cdot$m^2 depending on the class of target, a range resolution of 3000 m, a receiving array of 500-m length), the following is true.

- Big vessels (such as oil tankers and container ships) can be detected at a very long distance ($<$ 200 km) with a limited receiving aperture. Selection of a low-frequency carrier (4 and 8 MHz) makes the radar robust to sea roughness. Medium-sized boat (such as trawlers) can be detected at 6 MHz up to 100 km, if the range resolution does not exceed 1 km.
- Detection of small vessels is more problematic in bad sea state conditions (sea state $>$ 4). Target RCS is small compared to clutter patch RCS. Decreasing the frequency allows to reduce the clutter level but the ship RCS is also decreasing. A higher bandwidth (to improve the range resolution) and a higher antenna directivity are recommended to reduce the clutter area. All these factors are considered for the selection of a higher frequency to guarantee the detection of small ships at short and medium ranges (a few tens of kilometers).

This last analysis concerns slow ship targets; however, such cases might be not so realistic. For example, with regards to the case of smugglers, the use of go-fast boats (able to cope with bad sea state as well as to avoid detection by conventional radar) is more realistic. In this case, Doppler shift is higher, making the detection to be independent of the sea state.

TABLE I
REQUIREMENTS ON HFSWR ARRAY SIZE (SHIP <20 kn)

Target class	Sea state 1		Sea state 4	
	6 MHz	15 MHz	6 MHz	15 MHz
Oil tanker $\delta r = 5$ km	@370 km L$\sim$100 m	@370 km L$\sim$40 m	@370 km L$\sim$100 m	@370 km L$\sim$3700 m
Trawler $\delta r = 1$ km	@100 km L$\sim$500 m	@100 km L$\sim$200 m	@100 km L$\sim$500 m	@100 km L$\sim$20 km
Small Fast Boat $\delta r = 500$ m	@40 km L$\sim$1000 m	@40 km L$\sim$400 m	@40 km L$\sim$1000 m	@40 km -

Table I gives HFSWR requirements at different radar distances of interest (40, 100, and 370 km, depending on the target type) for a contrast ratio (TCR) of $+10$ dB. Note that L is the size of the receiving aperture (related to the azimuth resolution $\theta = \lambda/\mathrm{L}$) and δr is the required range resolution. For the numerical application, some orders of magnitude for the RCS are considered: 40 dB$\cdot$m^2 for an oil tanker, 20 dB$\cdot$m^2 for a trawler, and 10 dB$\cdot$m^2 for a small fast boat. The second-order reflectivity has been modeled using the simplified theory of Robson [3]. The reflectivity level is around -60 dB$\cdot$m^2/m^2 at 6 MHz (sea state 1 and 4) and at 15 MHz (sea state 1) and -40 dB$\cdot$m^2 at 15 MHz (sea state 4).

III. SIMULATIONS

To assess the capability of high-frequency waves to compensate for the shadow created in the X-band by big vessels, various simulations have been conducted.

The characteristic dimension of the ship is of the same order of magnitude as the emitted wavelength; we are, thus, in the resonance region and exact methods are required.

An integral representation of the field scattered by the ship has been used, solved thanks to a method of moment (MoM) code. The latter code is based on the one developed by Richmond (cf. [4] and [5]). It is designed for thin-wire structures.

As long wavelengths are of interest here, only big structures can be seen. Therefore, we have considered a rough model for the big ship, without any superstructure. It is of a trapezoidal shape, 15-m high (above the mean sea level), 12-m wide, 90-m long at the bottom, and 100-m long at the top.

For the excitation, a plane-wave model was used.

IV. SHADOW AREA BEHIND A LARGE SHIP

The object here is to study the diffraction effects of HF waves on big vessels, such as tankers, container ships, and so on. Using optic frequencies, a shadow area exists behind these ships. The aim is to study what happened at low frequencies. The representation of the propagated field shows the magnitude of the scattered field (not the total field) in the forward region (behind the object). It is normalized by the field that exists at these points without the ship. Thus, 0 dB means free propagation, i.e., there is no additional attenuation due to the ship. Fig. 3 shows maps of the vertical component of the electric field in a horizontal plane behind the ship, at three frequencies ($f = 3$, 10, and 18 MHz). Except for very small areas in the 18-MHz case, the attenuation is no more than 5 dB. For the 3-MHz case, there is almost no attenuation. The detection of SFB, the RCS of which is only a few dB$\cdot$m^2, could thus be possible.

Regarding the target-to-clutter ratio, the clutter can also be increased by a comparable amount. Therefore, the TCR is not going to be improved. But the aim here is not to try to improve the TCR, but to be able to detect the SFB; that is to have the target signal above the detection threshold of the radar.

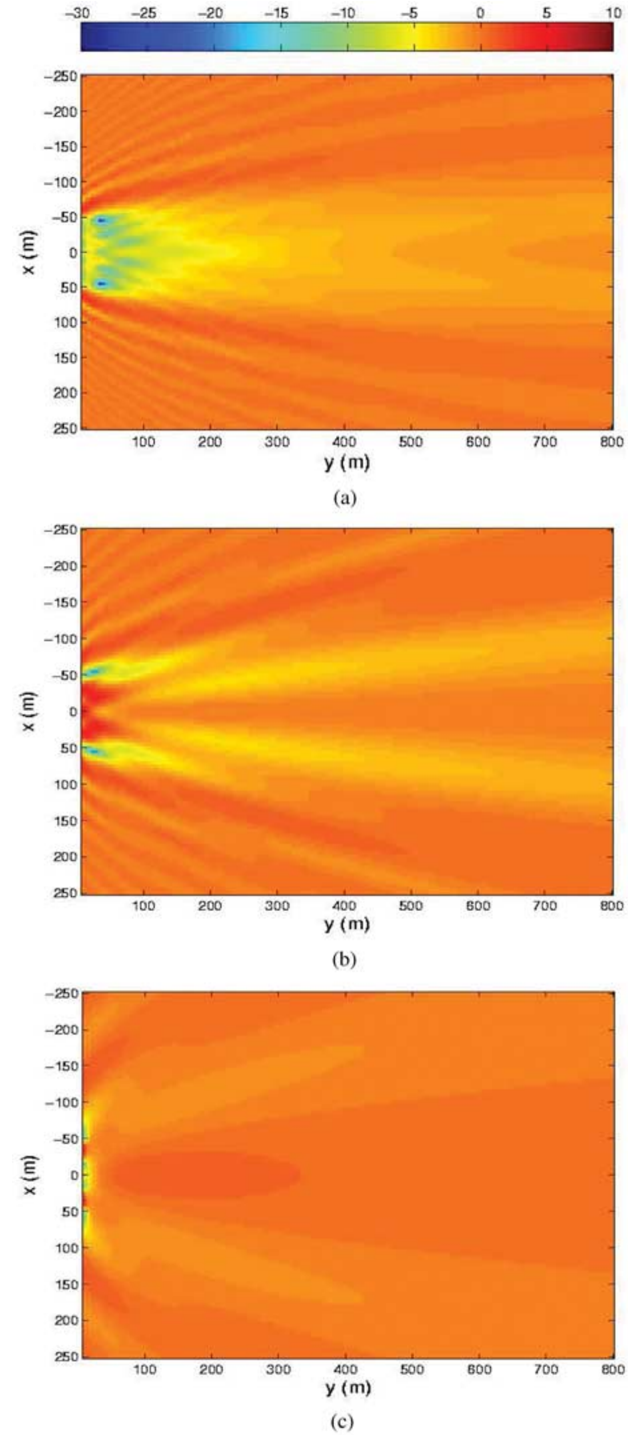

Fig. 3. Electric field behind the vessel, in the (x, y) plane, at (a) 18 MHz, (b) 10 MHz, and (c) 3 MHz. The vessel (100-m long) is along the x-axis, centered on 0. The incident plane wave is coming from $-y$.

V. ELECTROMAGNETIC INTERACTION BETWEEN A LARGE VESSEL AND AN SFB

According to the previous results, an SFB while having a very low RCS, could be detected with an HFSWR. To have an in-depth look at this problem, an SFB is added to our model and placed

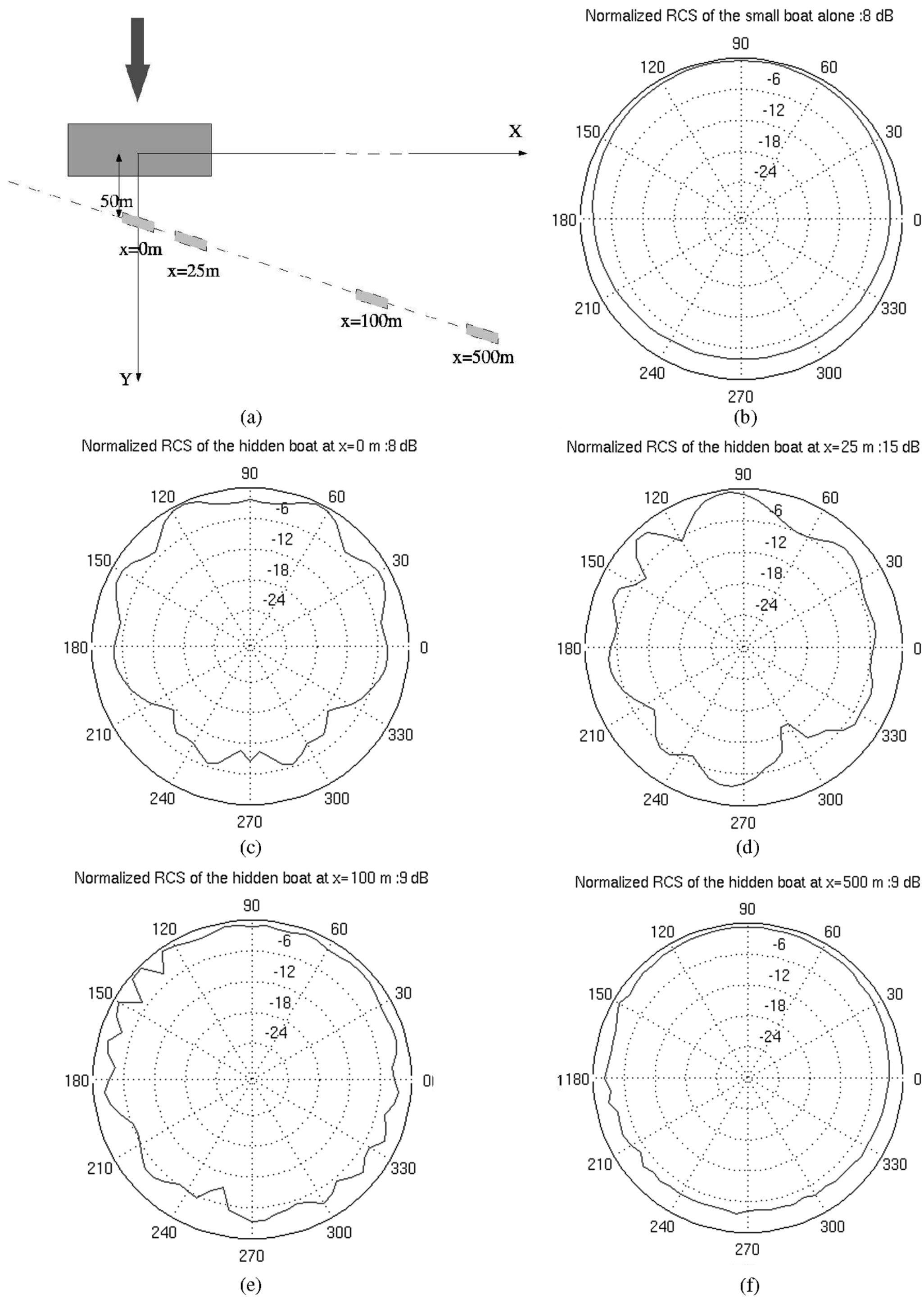

Fig. 4. Bistatic RCS of the SFB at 10 MHz, for various SFB positions. RCS amplitude normalization is indicated for each figure in the upper left corner. Positions of the SFB are taken from a trajectory of an SFB cruising behind the ship, at an angle of 20° with the ship direction. (a) Scene description. (b) RCS of an SFB not hidden. (c) RCS of an SFB hidden with $x = 0$ m. (d) RCS of an SFB hidden with $x = 25$ m. (e) RCS of an SFB hidden with $x = 100$ m. (f) RCS of an SFB hidden with $x = 500$ m.

behind the vessel. Simulations are conducted at 10 MHz for this new configuration, the SFB having different positions, all of them taken from a trajectory of an SFB cruising behind the ship, at an angle of 20° with the ship direction [cf. Fig. 4(a)]. At $x = 0$ m, the distance between the SFB and the vessel is 50 m. As an SFB, we consider a scaled version of a vessel, 6-m long. The incident plane wave is orthogonal to the broadside of the large vessel.

Fig. 4(b) shows the bistatic RCS of the SFB without any obstacle, while for Fig. 4(c)–(f), the big ship is included. The frequency is 10 MHz. The distance indicated is the abscissa of the SFB. Therefore, in Fig. 4(c) and (d), the SFB is hidden, while in Fig. 4(e) and (f), the SFB is directly illuminated. The RCS of the SFB, when hidden, is obtained by subtracting the RCS of the big ship alone from the RCS of the ensemble (big ship +

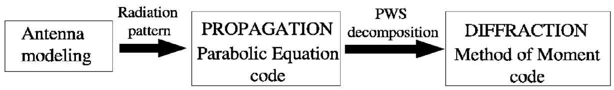

Fig. 5. Simulation architecture.

SFB). Referring to Fig. 3, the attenuation due to the big ship is very low at these positions.

Furthermore, another point has to be noted: For each figure, Fig. 4(c)–(f), the SFB is at different position. As a consequence, the average RCS varies from one position to another. However, the analysis of the results is not so straightforward. When the SFB is not hidden, the maximum of the RCS is in the backward direction. However, in the $x = 0$ m case, the maximum is not in the backward direction. For the $x = 25$ m case, the average RCS is much stronger than in any other cases, although the SFB is still hidden by the big ship. For instance, in the backward direction ($\theta = 90°$), in the $x = 0$ m case, the RCS is 5 dB; in the $x = 25$ m case (the SFB is still hidden), the RCS is about 14 dB; finally, for $x = 100$ m and $x = 500$ m cases (the SFB is no longer hidden), the RCS is 8 dB. The maximum RCS in the backward direction is, thus, obtained while the SFB is hidden, which is quite surprising. Actually, this is 6 dB more than without the big vessel. There is clearly an interaction (a constructive one in this case) between the two ships.

In the same way, considering Fig. 4(e) and (f), in both cases the SFB is not hidden. Nevertheless, in the $x = 100$ m case, there are still significant fluctuations in the RCS (maximum RCS is 8 dB and minimum RCS is about 0 dB), while in the $x = 500$ m case, the RCS is almost the same as for an SFB not hidden. The difference between the two cases is the distance to the big vessel.

Both constructive and destructive interactions have been assessed. An SFB, for a given position hidden behind a big ship, can then completely disappear or on the contrary have a very strong RCS, depending on the position of the receiver.

VI. Complete Simulation Tool

In the first part, a plane wave was used as an approximation of the excitation for the simulation. These simulations have shown both the validity of the use of HF waves for the detection of SFB in congested waters and the existence (and importance) of coupling effects between the SFB and big vessels.

For further practical use of this concept, the simulation tool has to account for the environment, i.e., the propagation conditions. This part will focus on the electromagnetic wave propagation above the sea surface. The technique used here is based on a parabolic equation (PE) code [6], [7] to treat the propagation over the sea surface, up to the vessel. It allows to take into account both natural obstacles (such as islands) and the roughness of the sea surface. The diffraction on the ships is still computed thanks to a MoM code. The hybridization of the two codes is realized through the decomposition in a plane-wave spectrum of the output of the PE code, which is used to generate the excitation voltage of an altered version of the MoM code. Fig. 5 gives a scheme of the corresponding architecture.

The PE code is first briefly described, then the hybrization technique is introduced.

A. PE Method

The PE method consists of approximating the Helmholtz wave equation with the assumption that the field propagates in a specific direction. Basically, the PE is, thus, a forward scatter, narrow-angle equation that inherently includes effects due to spherical Earth propagation, atmospheric refraction, and surface reflections. The PE code used here is computed by discrete mixed Fourier transform algorithm, which was defined to match the propagation algorithm to the impedance boundary condition. The propagation of surface waves, that is of interest here, requires an exact representation of surface impedance. For perfectly conducting surfaces, it has been shown [8] that a sine transform gives a solution satisfying the Dirichlet condition $u(x,0) = 0$ for $x > 0$ and that a cosine transform leads to a solution verifying the Neumann condition $\partial u/\partial z(x,0) = 0$.

Kuttler and Dockery [9] have then shown that (2) can be used to express any boundary condition

$$\left.\frac{\partial u}{\partial z}\right|_{z=0} + \alpha u(z=0)|_{z=0} = 0 \tag{2}$$

where

$$\alpha = ik\sin\theta_i\left(\frac{1-\Gamma}{1+\Gamma}\right) \tag{3}$$

where Γ is the Fresnel reflection coefficient and θ_i is the elevation angle.

The idea is then to use a transform that can propagate automatically a solution matching these impedance boundary conditions. This is the discrete mixed Fourier transform algorithm, introduced by Kuttler and Dockery [9], [7].

B. Hybrid Technique

A direct fast Fourier transform (FFT) is performed on the output field of the PE, along a vertical direction

$$\mathcal{W}(k_x,z) = \frac{1}{2\pi}\sum E(x,z)\,e^{jk_x x}$$
$$\text{where}\begin{cases} k_x = k_0\sin(\psi) \\ \psi : \text{orientation angle.}\end{cases} \tag{4}$$

As for the plane-wave spectrum technique [10], the result $\mathcal{W}$ can be viewed as a weighted sum of plane waves with their directions ψ given by the wave number. These weights can then be used to express the field in the spatial domain as

$$\vec{E}(x,y,z) = \sum_{n=1}^{N}\mathcal{W}(k_x,z)\,e^{-jk_x x}. \tag{5}$$

Fig. 6 illustrates this idea.

Although the parabolic equation code is a two-dimensional (2-D) code, the results are considered as three-dimensional (3-D). Actually, because of the long propagation distance in our problem (especially with regards to the wavelength) and of the small size of the maps (such as the ones in Fig. 3), the variation of the spectrum along the third direction are small enough and will be ignored. This means that computation of the PE code is limited to a 2-D scene and takes a zero value for the second direction angle of all the plane waves. A normalization

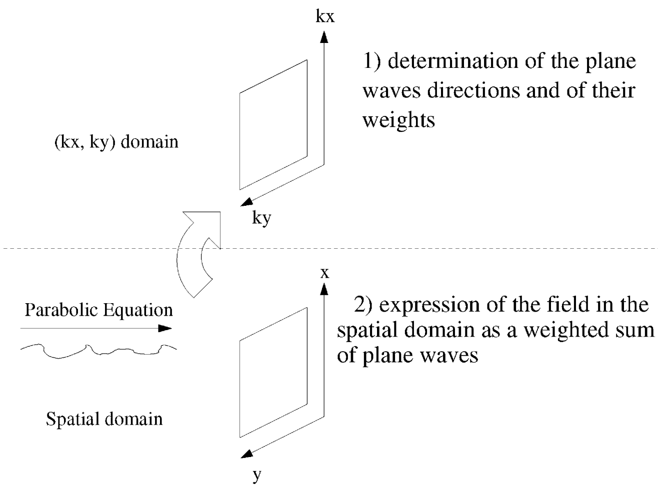

Fig. 6. Principle of the decomposition of the field as a weighted sum of plane waves. The propagation part is computed with a PE code, the diffraction one with a MoM code.

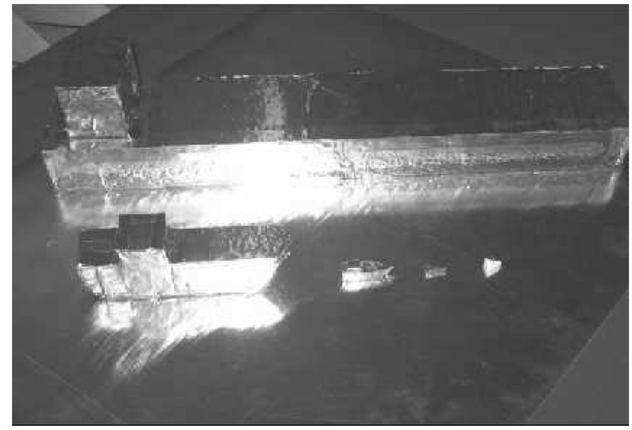

Fig. 7. View of the various scaled targets for anechoic chamber measurements.

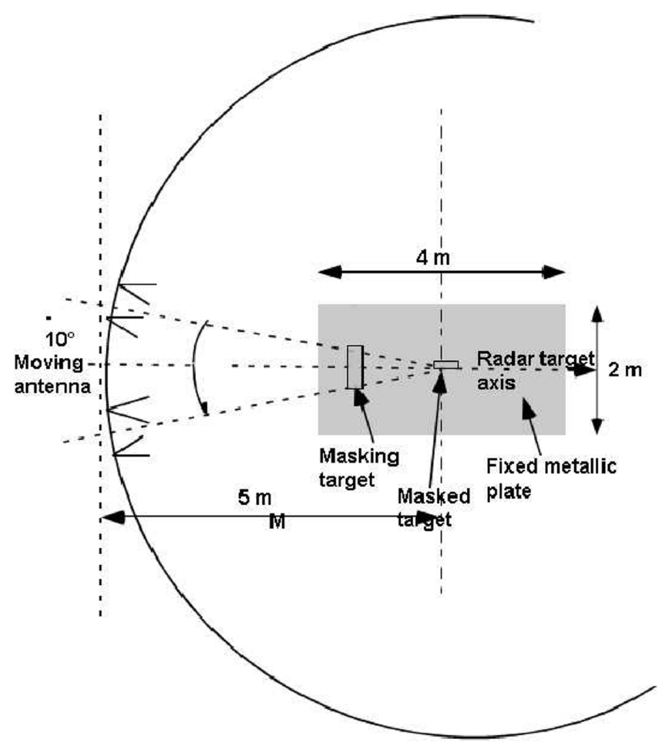

Fig. 8. Measurements configuration for anechoic chamber measurements.

coefficient is just used to take into account the projection from 2-D to 3-D.

Finally, that weighted sum of plane waves is used to generate the excitation voltage of the MoM.

An interesting feature of this hybrid technique is that the implementation is simple and the computation is quick. It only requires one FFT. In the same way, the second part of the technique (the complex excitation of the MoM) is not time-consuming because it only involves linear operations.

C. Summary

Through the use of the PE method, complex propagation effects can be taken into account. Dockery and Kuttler [7] have demonstrated the validity of the PE to compute surface wave propagation. They have compared PE results to a mode theory surface wave model, using Barrick's rough-surface impedance model [11], [12] to modify α. PE results are also valid over inhomogeneous paths, as demonstrated in [8].

VII. Measurements

A. Measurements Configuration

Measurements have been performed to study the shadow effect in HF-band from scaled model. Scaled models of different sizes (tanker, container ship, SFB, and fishing boat) were considered with a scale factor equal to $1:500$. Scaled targets were placed on a metallic plate. Fig. 7 gives a global view of the different targets. Measurements were performed in the anechoic chamber at Office National d'Etudes et de Recherches Aérospatiales (ONERA), the French aeronautics and space research center, according to the configuration shown on Fig. 8. The bistatic angle (between the transmitting and receiving antenna 4°) is much smaller than the expected beamwidth presented by the targets RCS pattern, then this configuration can be considered as monostatic. Data were collected in the 2–15-GHz band corresponding to 4–30-MHz band for scale $1:1$ targets. A short dipole antenna was also used to measure the field in the shadow of the masking object. After calibration, collected data were analyzed to obtain the following: a) the RCS pattern of the different ships, b) the attenuation of propagation due to the masking ship, and c) the inverse synthetic aperture radar (ISAR) image of the targets, after processing of the data collected for different position of the radar antenna.

To form an ISAR image, we have a moving target, not a moving radar (contrary to SAR image). This is especially useful in an anechoic chamber, where the antenna is then moving on a rail.

Fig. 9 shows the attenuation measured with a dipole antenna in the shadow of the tanker. Referring to Fig. 4(a), the dipole is located at $x = 0$ m, and we move it along the y-axis, thus increasing the separation distance between the masking ship and the dipole. The dimensions (scale $1:1$) of the tanker are: $L =$

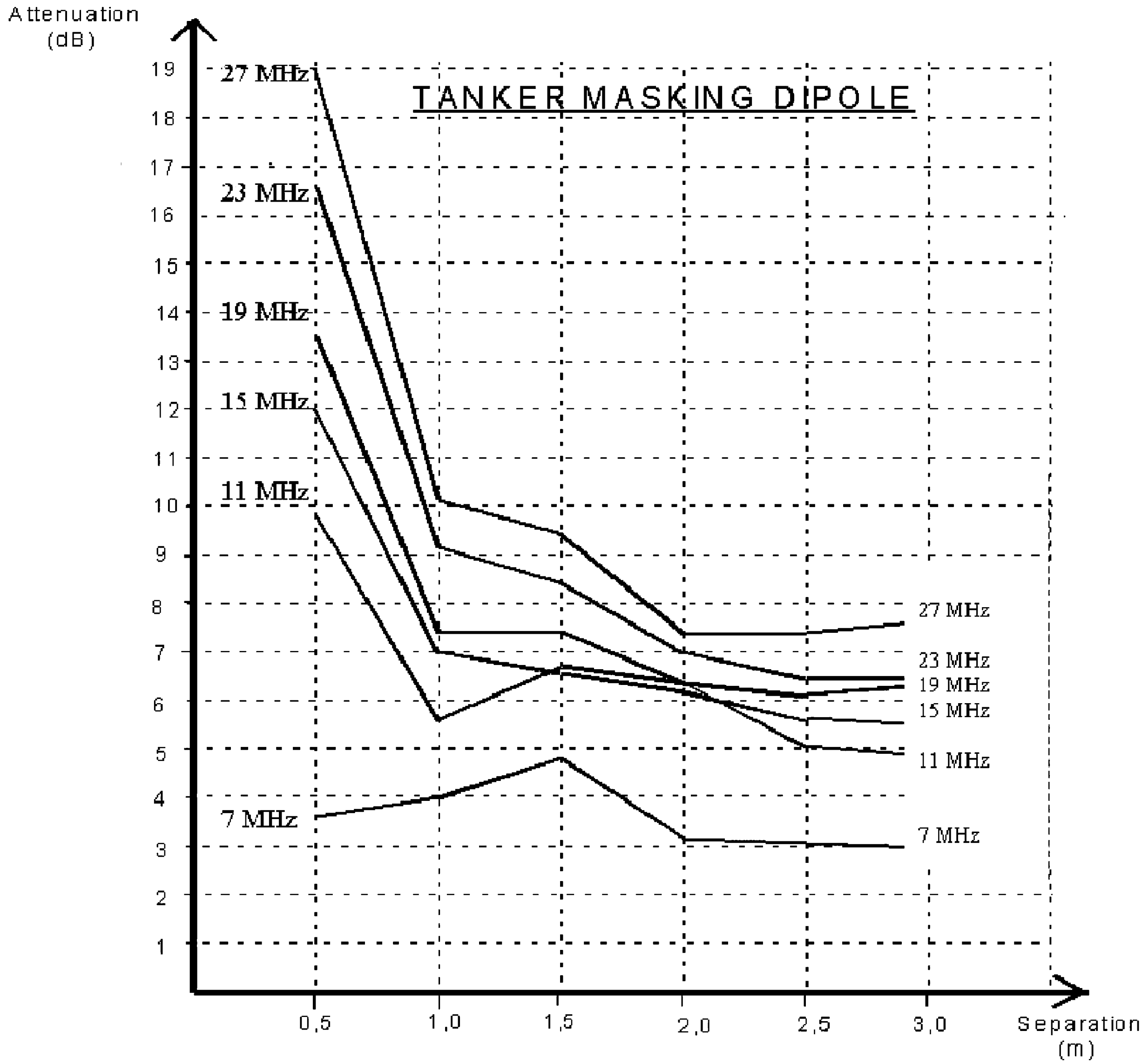

Fig. 9. Effect of the separation distance (y-axis) for a tanker masking a dipole.

250 m, $W = 50$ m, $h = 25$ m. Data have been averaged in different bandwidths to improve the quality of measurements. The measurements were made in a backscattering mode, i.e., the attenuation was derived from measuring the RCS of the dipole. A set of measurements was performed to derive the RCS values as well as the attenuation due to the masking vessel as follows:

a) measurement of the plate alone (without any object);
b) measurement of the plate with the masking vessel;
c) measurement of the plate with only the dipole;
d) measurement of the plate with the masking vessel and the dipole.

The first phase a) allows for measuring the anechoic chamber in presence of the metallic plate. The coherent difference between b) and a) measurements gives the estimation of the masking vessel RCS. By the same way, by subtracting a) measurements from other measurements c) and d), we can obtain the RCS of the dipole with or without the presence of the masking vessel. Also, the attenuation due to masking vessel can be directly obtained by computing the difference of RCS level between c) and d). In the frequency band of interest 2–15 GHz, use of subbands (of typically 1 or 2 GHz), combined with a rotation of transmitting and receiving antennas (within an interval of $\pm 10°$) has been considered to provide high-resolution imaging of the targets. Through this high resolution, it has been possible to separate the RCS contributions from the masking object and the dipole.

B. Results Analysis

Results of RCS measurements are presented in this section. As measurements were performed on $1:500$ scaled model (from 2 to 15 GHz), the level in decibel of RCS should be increased to 54 dB to represent the RCS of realistic target in the HF-band (from 4 to 30 MHz). Each target (dipole, SFB, and fishing boat) is analyzed in association with each of the two available masking objects (container ship and tanker). The figures represent the RCS (versus frequency) for the target itself (without any masking object), the RCS of the target in a masking configuration, and also the difference between the two

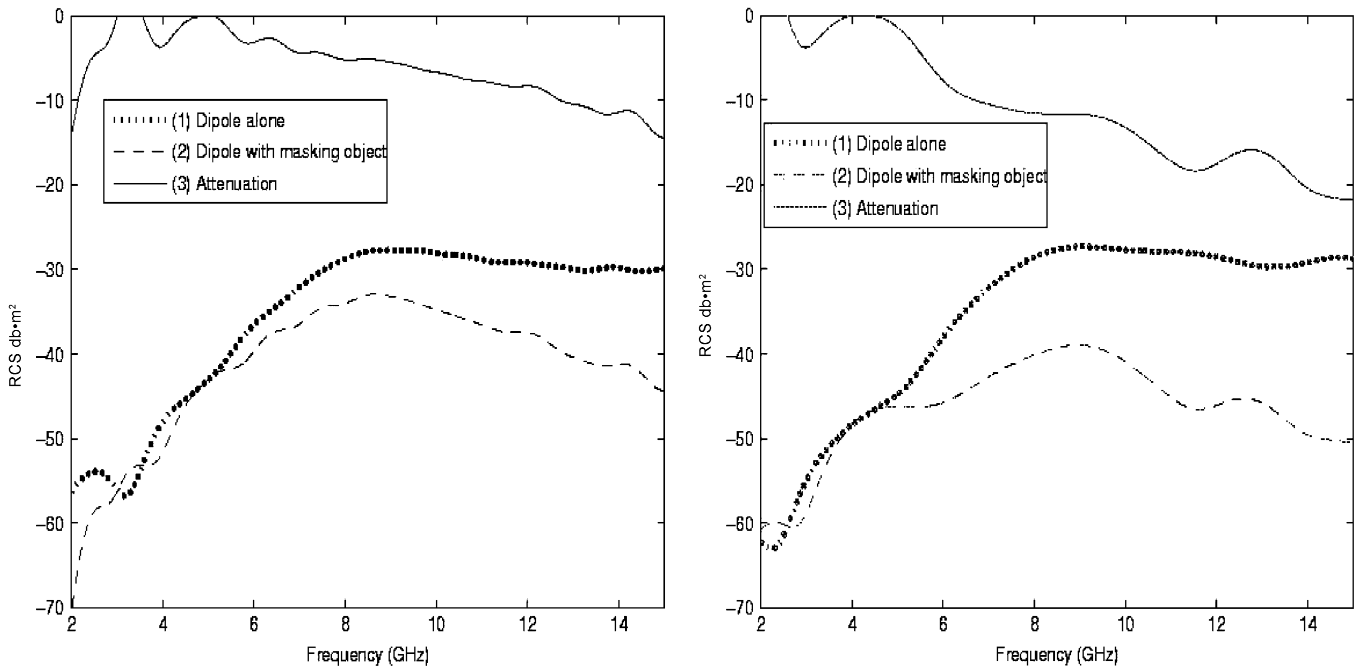

(a) (b)

Fig. 10. RCS (dB·m^2) versus frequency for Dipole. (a) Masked by a container ship. (b) Masked by a tanker.

RCS measurements, which can be interpreted as the attenuation resulting from the presence of the masking object.

A set of various separation distances, between the target and the masking object was considered in the trial campaign (from 50 cm up to 3 m, which corresponds to 250 up to 1500 m in real condition). We only consider here the minimum separation distance equal to 50 cm. Note that below this separation distance, the measurement of target RCS is very difficult. The reason comes from the stronger RCS level of the masking object itself (50 dB or more in some cases) making problematic the separation in distance of the masking and target objects (even with a range resolution of a few centimeters). In real conditions, we can think of exploiting the Doppler effect of the target (higher or significantly different from the Doppler effect of the masking object) to perform the separation of the two echoes.

Fig. 10 gives the RCS of a short dipole. The (1) curve in the two figures is the RCS level of the dipole without any masking object. The two curves must be theoretically identical. However, we can see some differences in the lower band below 4 GHz. These differences are due to the poor sensitivity of the measurements when the RCS is lower than -50 dB·m^2. Then, we will pay attention to the interpretation of the results in this part of the curves, especially when the level is lower than -50 dB·m^2.

The RCS of the dipole raises its maximum value between 8–9 GHz, which corresponds to a quarter wavelength of 8.83 mm (over a metal plane).

When the container is masking the dipole [cf. Fig. 10(a)], the attenuation of RCS is a monotonic function of the frequency. The average slope of the attenuation function is equal to -1 dB/GHz, This attenuation corresponds to -0.5 dB/MHz in HF-band between 6–30 MHz.

Then, the tanker is masking the dipole [cf. Fig. 10(b)], the attenuation curve presents several large fluctuations. The explanation is quite simple: With a larger size the tanker provides a masking interaction which is highly frequency-dependent.

Fig. 11 shows the same kind of results when the target is an SFB. However, in this case, the evolution of the RCS is more complex. Target size is greater than the wavelength, providing several oscillations of the target RCS itself. Behind a smaller masking object (i.e., container) the RCS curve is affected with the same monotonic function as previously. Behind the tanker, the RCS is affected with several fluctuations due to the resonant diffraction pattern of the masking object. In both cases, as the attenuation is higher in the upper band, it becomes interesting to operate in lower band when the target is masked.

The same kind of behavior is observed when the target is a fishing boat (cf. Fig. 12). With a greater size than the previous target, the RCS curve (free space) presents stronger fluctuations. Between 4.5–6.5 GHz, the RCS level is over -30 dB·m^2 (between 9–13 MHz, 24 dB·m^2 in HF-band). The same frequency interval remains interesting to be used with an RCS level superior to -36 dB·m^2 behind the tanker (18 dB·m^2 in HF-band) and to -31 dB·m^2 behind the tanker (23 dB·m^2 in HF-band).

VIII. Conclusions and Perspectives

The detection of SFB in itself is a hard issue, as they are low RCS targets. When they are behind big vessels, this detection becomes impossible if only microwave frequencies are considered. We have investigated here an alternative solution: the use of the HF-band. In this case, the characteristic dimension and the wavelength are of the same order of magnitude. In a first part, resonant effects have been demonstrated: The total electromagnetic field behind the big vessel is almost not affected by the vessel, as long as the considered location is not stuck to the vessel. The shadow zone that exists in X-band is no longer present with the HF-band.

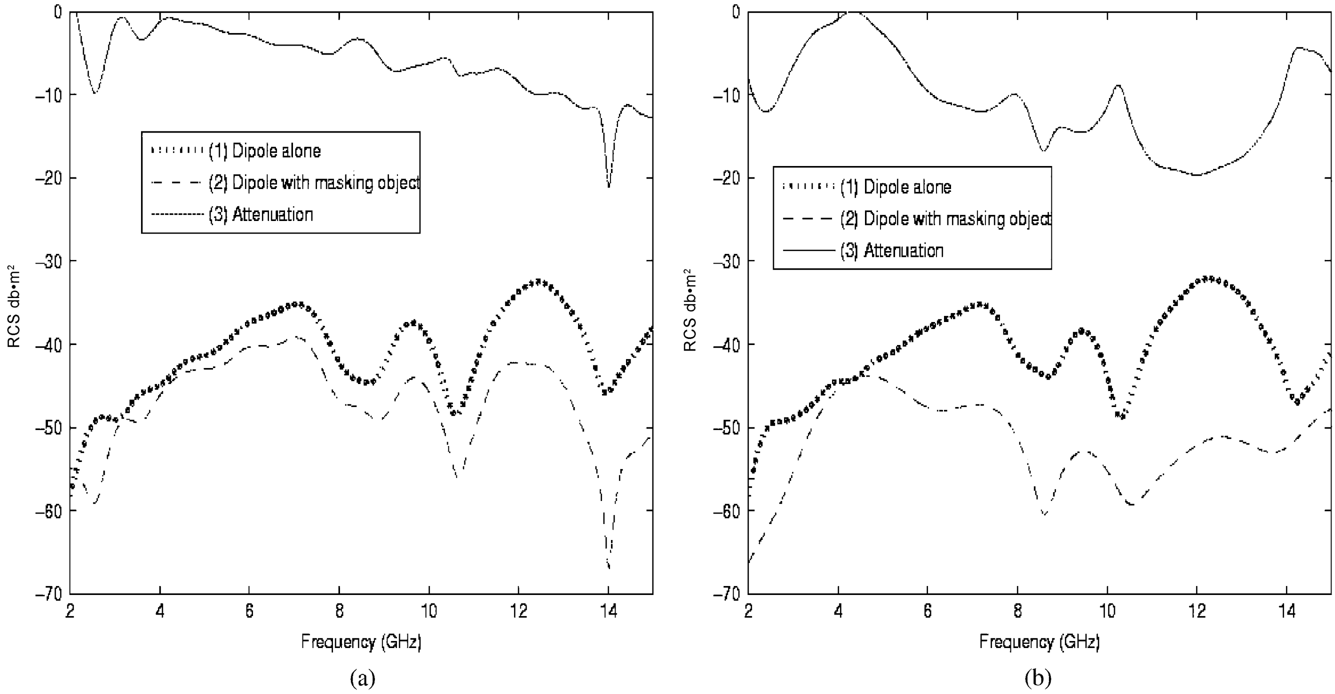

Fig. 11. RCS (dB·m^2) versus frequency for SFB. (a) Masked by a container ship. (b) Masked by a tanker.

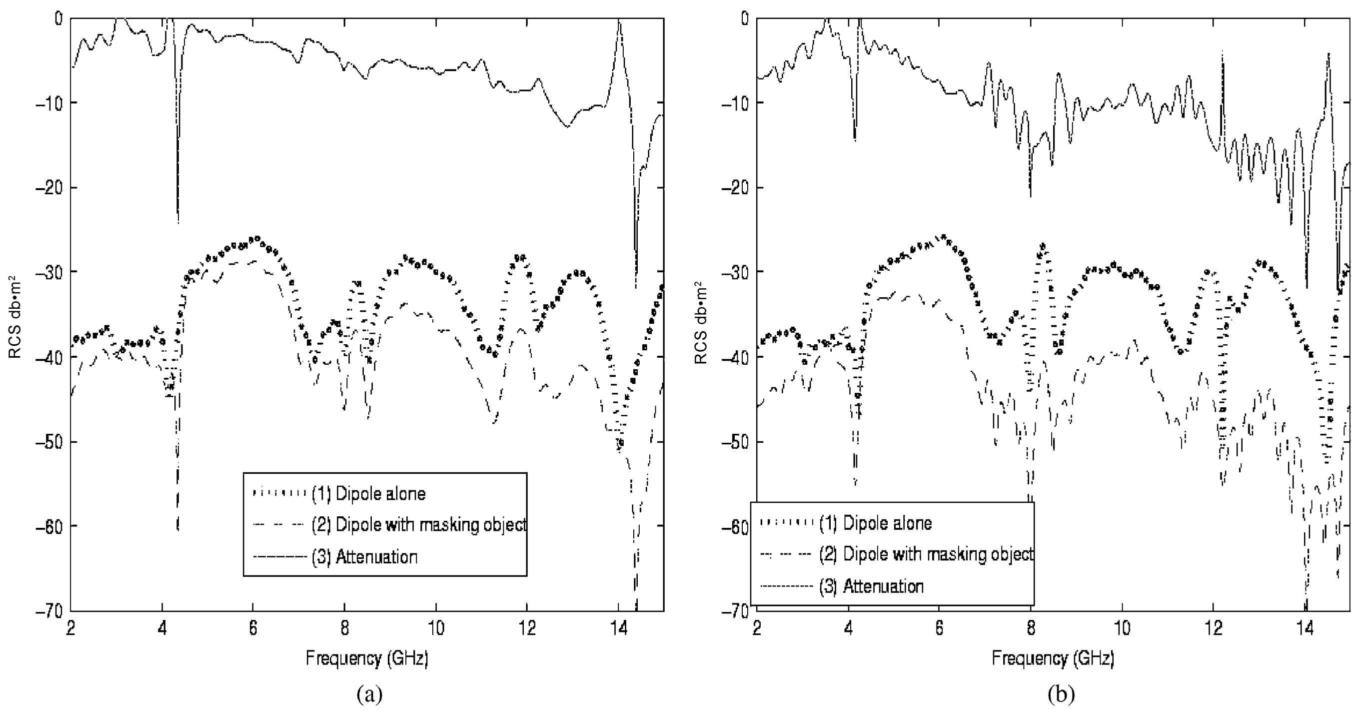

Fig. 12. RCS (dB·m^2) versus frequency for Fishing boat. (a) Masked by a container ship. (b) Masked by a tanker.

This has been validated through anechoic chamber measurements for various masking and hidden objects. In a second part, we have investigated the effect of the big vessel on the RCS of the SFB. Results of the first part have been confirmed: When there is no attenuation behind the vessel, the RCS of the hidden SFB is roughly the same as when the SFB is not hidden. Besides, a very interesting effect has also been demonstrated: coupling effects between the big vessel and the SFB. These can lead to RCS fluctuations of more than 20 dB, either completely masking the SFB or giving it the RCS of a quite big ship.

A complete simulation tool has also been introduced, that accounts for the environmental effects and for complicated paths. Now that this concept has been validated, further works will consist of studying and developing the necessary algorithms for the analysis of the signal.

REFERENCES

[1] "Piracy takes higher toll of seamen's lives" Piracy_report_2003.asp., Jan. 2004 [Online]. Available: http://www.dockwalk.com/issues/2004/march/piracyl.shtml

[2] P. Broche, P. Forget, J. C. de Maistre, J. L. Devenon, and M. Crochet, "VHF radar for ocean surface current and sea state remote sensing," *Radio Sci.*, vol. 22, no. 1, pp. 69–75, Jan.–Feb. 1987.

[3] R. E. Robson, "Simplified theory of first and second order scattering of HF radio waves from the sea," *Radio Sci.*, vol. 19, no. 6, pp. 1499–1504, Nov.–Dec. 1984.

[4] J. Richmond, "Radiation and scattering by thin-wire structures in the complex frequency domain" NASA, Tech. Rep. CR-2396, May 1974.

[5] ——, "Computer program for thin-wire structures in a homogeneous conducting medium NASA, Tech. Rep. CR-2399, Jun. 1974.

[6] G. Dockery, "Modeling electromagnetic wave propagation in the troposphere using the parabolic equation," *IEEE Trans. Antennas Propag.*, vol. 36, no. 10, pp. 1464–1470, Oct. 1988.

[7] G. Dockery and J. R. Kuttler, "An improved impedance-boundary algorithm for Fourier split-step solutions of the parabolic wave equation," *IEEE Trans. Antennas Propag.*, vol. 44, no. 12, pp. 1592–1599, Dec. 1996.

[8] M. Levy, *Parabolic equation methods for electromagnetic wave propagation*. London, U.K.: The Institution of Electrical Engineers, 2000.

[9] J. R. Kuttler and G. Dockery, "Theoretical description of the parabolic approximation/Fourier split-step method of representing electromagnetic propagation in the troposhere," *Radio Sci.*, vol. 26, no. 2, pp. 381–393, Mar.–Apr. 1991.

[10] P. Clemmow, *Plane Wave Spectrum Representation of Electromagnetic Fields*. New York: Pergamon, 1966.

[11] D. Barrick, "Theory of HF and VHP propagation across the rough sea 1: The effective surface impedance for a slightly rough highly conducting medium at grazing incidence," *Radio Sci.*, vol. 6, pp. 517–526, 1971.

[12] ——, "Theory of HF and VHF propagation across the rough sea 2: Application to HF and VHF propagation above the sea," *Radio Sci.*, vol. 6, pp. 527–533, 1971.

Régis Guinvarc'h (S'02–M'04) received the engineering degree and the M.S. degree in 2000 and the Ph.D. degree [with a Les Conventions Industrielles de Formation par la Recherche (CIFRE) grant] in 2003, all in electrical engineering from Instituts Nationaux des Sciences Appliquées (INSA), Rennes, France.

From 2000 to 2003, he was with the Etienne Lacroix company, France, as a Research Engineer, where he was engaged in research on microwave remote sensing through discrete random media. Since 2004, he has been with the Supelec ONERA NUS DSTA Research Alliance (SONDRA), Gif-Sur-Yvette, France, where he is working on conformal antennas and HF surface wave radar.

Marc Lesturgie received the engineering degree from Ecole Nationale Suprieure de l'Aronautique et de l'Espace (ENSAE), Toulouse, France, in 1985, the M.S. degree (DEA) in electronic and microwave from University of Toulouse, Toulouse, France, in 1986, and the Research Directorship Habilitation from the University of Paris VI, Paris, France, in 2005.

In 1987, he joined Office National d'Etudes et de Recherches Aérospatiales (ONERA) as a Research Engineer and worked in a wide range of low frequency and new concepts of bistatic and multistatic radars. From 1996 to 2000, he was the Head of New Radar Concepts team. Currently, in charge of radar prospective for ONERA, he is also the Director of Supelec ONERA NUS DSTA Research Alliance (SONDRA), Gif-Sur-Yvette, France, a joint laboratory established between Supelec, ONERA, the National University of Singapore, and the Defence Agency of Singapore. He is the author and coauthor of over 25 journal and conference papers, several patents, and over 40 technical reports.

Mr. Lesturgie he has been a Chairman of the SEE/Committee 23 (radio-location and navigation) since 2000. He has organized several international conferences and acted as the Technical Chairman of the *International Conference on Radar Systems* in 2004.

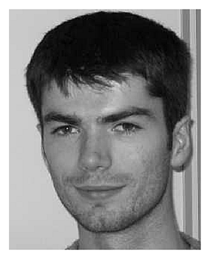

Rémi Durand received the engineering degree from ISEP and the M.S. degree in electrical engineering from Telecom Paris VI, Paris, France, both in 2004. He is currently working towards the Ph.D. degree at Supelec ONERA NUS DSTA Research Alliance (SONDRA), Gif-Sur-Yvette, France.

His research interests are in electromagnetic scattering and signal processing.

Anil Cheraly is in charge of the measurements at the testing facilities CAMERA2 and BABI of Office National d'Etudes et de Recherches Arospatiales (ONERA).